# GLAD Pt−Ni Alloy Nanorods for Oxygen Reduction Reaction

Nancy N. Kariuki,*,[†] Wisam J. Khudhayer,[‡] Tansel Karabacak,[§] and Deborah J. Myers[†]

[†]Chemical Sciences and Engineering Division, Argonne National Laboratory, Argonne, Illinois 60439, United States
[‡]Department of Electrochemical Engineering, University of Babylon, Babylon 51002, Iraq
[§]Department of Applied Science, University of Arkansas at Little Rock, Little Rock, Arkansas 72204, United States

ABSTRACT: Vertically aligned platinum−nickel (Pt−Ni) alloy nanorod arrays were grown on glassy carbon electrodes using a magnetron sputtering glancing angle deposition (GLAD) technique. X-ray diffraction and electron microscopy results show that the as-deposited nanorods are alloys and that the alloy composition and geometric properties of Pt−Ni nanorods can be changed by controlling the GLAD deposition parameters. The GLAD Pt−Ni nanorod electrodes were investigated as potential electrocatalysts for the oxygen reduction reaction (ORR) in polymer electrolyte fuel cells (PEFCs) using cyclic voltammetry (CV) and rotating-disk electrode (RDE) techniques in aqueous perchloric acid electrolyte. The electrochemically active surface area (ECA), determined from the charge for hydrogen adsorption and desorption in the CVs, was estimated to be a factor of 3 or more larger than the geometric surface area of the nanorods. The ORR mass-specific activity of the Pt−Ni nanorods was found to be a factor of 2.3−3.5 higher than that of pure Pt nanorods of the same dimensions and increase with increasing Ni content, whereas ORR area-specific activity enhancement was only observed for the nanorods with the highest Pt content. In addition, the Pt−Ni nanorods were found to have higher stability against loss of ECA during potential cycling than Pt nanorods and conventional high-surface-area-carbon-supported Pt nanoparticles.

KEYWORDS: glancing angle deposition (GLAD), Pt−Ni nanorods, oxygen reduction reaction (ORR), nanostructured electrocatalysts, Pt−Ni alloy catalyst, polymer electrolyte fuel cells
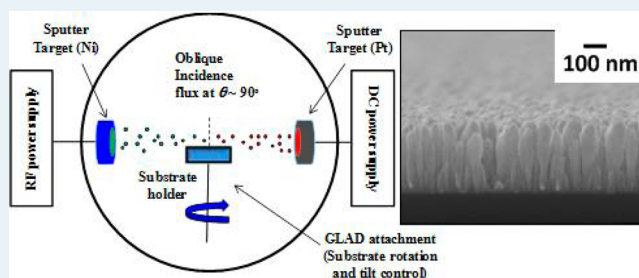
INTRODUCTION

Polymer electrolyte fuel cells (PEFCs) must meet demanding performance, durability, and cost targets if commercialization for transportation applications is to be successful.[1,2] The dominant initial voltage losses and voltage decay with operating time in state-of-the-art membrane-electrode assemblies (MEAs), with electrodes comprised of platinum catalyst nanoparticles (3−5 nm diameter) supported on high-surface-area carbon black (Pt/C), are attributed to the slow kinetics of oxygen reduction reaction (ORR) on the cathode electrocatalyst and loss of Pt nanoparticle electrochemically active surface area (ECA), respectively.[1−4] Besides the issues associated with Pt, there are additional performance issues related to the carbon support, including oxidation of the carbon,[5] formation of peroxide species leading to degradation of the polymeric membrane, and separation from the ionomer leading to loss of catalyst ECA.[6] Due to these limitations, extensive efforts are focused on the development of high-performance, low-Pt-content, durable, and carbon-free catalysts with stable support materials.[7−12] Many studies in the literature have been devoted to Pt-based alloy systems with or without electrochemical[13,14] or chemical[14,15] dealloying to increase the intrinsic ORR activity of Pt through modification of its structural and electronic properties.[13,16−21] Another route being pursued to reduce Pt loading is the translation of the intrinsically higher activity of extended surfaces[22] to structures with the required volumetric density of active sites, scalability, and economic viability for fuel cell applications.[23]

The 3M Company has demonstrated greatly enhanced activity and durability of nanostructured thin film (NSTF) electrocatalysts composed of large-grained polycrystalline Pt or Pt alloy thin films deposited on and encapsulating oriented crystalline whiskers of an organic pigment.[12,24−26] The low volume of the organic pigment catalyst support, relative to Pt/C, results in electrodes that are over an order of magnitude thinner than traditional Pt/C-based electrodes with equivalent Pt loading, which is both a benefit and challenge of this design. The challenge arises in the high volumetric rate of water production which can lead to issues with water accumulation and freezing during transients and low-temperature start-up, respectively.[27] Another issue inherent in the NSTF electrocatalysts is the likely decomposition of the organic whisker support, which limits the processing of these materials at higher temperatures.[24,28,29] Thermal annealing has been demonstrated to induce subsurface Pt to segregate to the surface, forming a core−shell in Pt−base metal alloy catalysts leading to enhancement of catalytic activity.[17,20,21,29]

The design of non-supported nanostructures of Pt and Pt alloys of controllable size, composition, and morphologies could address some of the issues inherent in supported thin film structures (e.g., 3M's NSTF catalysts) and also impart catalytic enhancement based on the ability to control the surface termination to the most active crystal planes for ORR. New architectures of interest, including porous or non-porous one-dimensional nanostructures, have been produced using a variety and/or combination of chemical, electrochemical, and electrospinning methods.[30−34] Common problems with porous nanostructured catalysts include diffusional resistance encountered by reactants and products that have molecular dimensions similar to those of the porous nanostructures as well as failure of long, continuous, one-dimensional nanostructures to stand alone without a support.[30,31] Porous nanostructures based on ordered arrays of vertically aligned one-dimensional nanorods deposited on engineered three-dimensional substrates represent an interesting possibility to develop improved catalysts. In a specific example, arrays of nanorod structures with a well-controlled surface morphology can be grown using a simple physical self-assembly technique known as glancing angle deposition (GLAD) in which a vaporized particle flux arrives at the substrate from an oblique angle of incidence. During GLAD, there is a preferential growth on the islands of higher height due to a "shadowing effect" of the obliquely incident flux of atoms, which leads to the formation of isolated nano-structured geometries.[35] Bonakdarpour et al.[8] fabricated columnar titanium structures on smooth glassy carbon (GC) disks using GLAD. Gasda et al. deposited platinum catalyst layers onto gas diffusion layer (GDL) substrates[36] by GLAD and tested them as cathodes in PEFCs. They have extended this approach to normal-incidence-angle-deposited Pt on chromium nitride (CrN) nanoparticles,[7] patterned carbon nanorods,[37] and electrochemically etched carbon nanorod array supports.[38] The design and fabrication of multicomponent nanostructures with different morphologies by GLAD have been reviewed by He and Zhao.[39] More recently, we have used the GLAD technique to grow vertically aligned Pt nanorods[11] and Pt thin films coated on Cr nanorods.[9] These nanorod structures were supported on glassy carbon for evaluation of ORR activity using the rotating-disk electrode technique and aqueous acidic electrolyte. Our studies showed enhanced ORR activity and stability of GLAD Pt nanorods compared to conventional Pt/C catalysts. The enhanced activity was attributed to large crystallite size, single-crystal property, and the dominance of Pt ⟨110⟩ crystal planes on the nanorod sidewalls,[10,11] reported to be the most active face for ORR in perchloric acid electrolyte.[10,11,17,40]

By utilizing GLAD, it is furthermore possible to grow multicomponent nanostructures by incorporating multiple sources of materials in the deposition system.[39,41−43] In addition to high catalytic performance and low-cost requirements, large-scale automotive fuel cell commercialization requires the manufacture of catalyst electrodes at high rates approaching several MEAs per second.[23] Roll-to-roll processing utilizing oblique deposition has been used for several decades, and several variations of oblique metal evaporation for roll-to-roll systems have been explored.[44] Moving GLAD to a roll-to-roll system will enable GLAD nanostructures to be realized in a high throughput environment.

In this paper, we have used the GLAD technique to fabricate Pt−Ni alloy nanorod array electrocatalysts on glassy carbon substrates for evaluation of the electrocatalytic ORR activity.

Scanning electron microscopy (SEM), energy dispersive X-ray (EDX), and X-ray diffraction (XRD) methods were utilized to study the morphology, elemental composition, and crystallo-graphic properties of the Pt−Ni nanorods, respectively. Cyclic voltammetry (CV) and rotating disk electrode (RDE) experiments were performed at room temperature in dilute perchloric acid electrolyte to characterize the ORR activity and activity stability of the Pt−Ni nanorods.

■ EXPERIMENTAL SECTION

Pt−Ni nanorods were synthesized by the magnetron sputter GLAD technique (Excel Instruments, India) in an ultrahigh vacuum system with a base pressure of 7.5×10^{-7} Torr. The base pressure was achieved using a turbo-molecular pump backed by a mechanical pump. The substrates were glassy carbon (GC) disk inserts (5 mm OD × 4 mm thick, Pine Instrument, NC) and silicon (Si) wafer pieces. The nanorod arrays coated on Si substrates were utilized for SEM, EDX, and XRD analyses. The GC disk inserts and Si substrates were mounted, at the same time, on a sample holder located approximately 12 cm away from Pt and Ni sputter targets (i.e., disk-shaped sources) of diameters 2.54 and 5.08 cm, respectively. An RF power supply was used to generate the plasma for the Ni target, while a DC power was used for the Pt. Pt−Ni nanorods were co-deposited by placing the substrate at an ~90° oblique angle with respect to the two sputter sources of Pt and Ni (see Figure 1). We note that the actual deposition
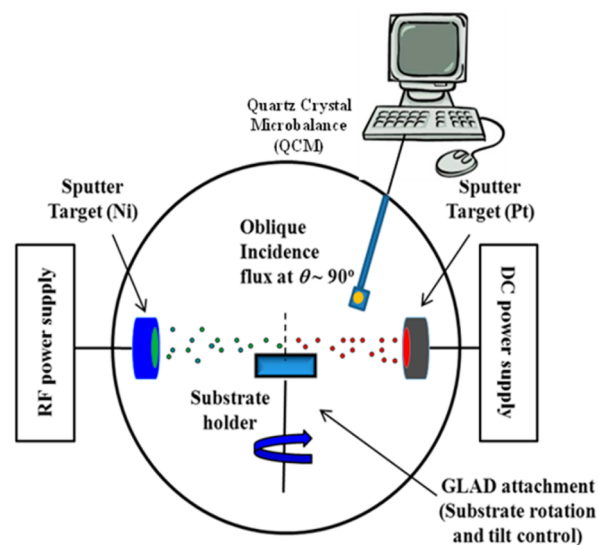
Figure 1. Schematic of the glancing angle deposition (GLAD) technique used for the fabrication of Pt−Ni alloy nanorod arrays using a co-deposition configuration.

angle on the substrates is believed to be at least a few degrees smaller than 90° due to the relatively large size of the sputter targets and angular distribution of the incident flux of Pt and Ni atoms. The substrates were attached to a stepper motor and rotated at a speed of 5 rpm around the substrate-normal axis for growing vertical nanorods. During deposition, the RF power was maintained at 300 W for Ni, while for Pt the DC power was set to 50, 100, 150, and 200 W for the deposition of nanorods with Pt to Ni atomic ratios of 1:8, 1:3, 1:2, and 1:1, respectively. The working gas was ultrahigh purity Ar (99.99%) at a pressure of 3.15 mTorr. Growth time was varied and was 35, 28, 22, and 18 min for Pt to Ni atomic ratios of 1:8, 1:3, 1:2,

and 1:1, respectively, to obtain nanorods with approximately similar length and diameter for the different Pt to Ni atomic ratios.

The freshly prepared samples were characterized using a quartz crystal microbalance (QCM, Inficon Q-pod QCM monitor, crystal: 6 MHz gold coated standard quartz), XRD (Bruker D8 discover), and a field emission scanning electron microscope (FESEM) (FESEM-6330F, JEOL Ltd., Tokyo, Japan) with EDX capability. For the QCM measurements, the Pt nanorods were deposited, in a separate run prior to the co-deposition of Pt−Ni nanorods, directly on quartz crystal substrates to determine the Pt loading by comparing the oscillation frequencies of the blank and the coated crystal. During the co-deposition of Pt and Ni, the QCM attachment (see Figure 1) was facing the Pt target to monitor the progress of the deposition, taking into consideration a distance correction factor between the QCM and the sample holder. The Pt deposition rate was further confirmed using SEM analysis to measure the length of the nanorods after various deposition times. The XRD measurements were performed at 40 kV and 35 mA using Cu Kα radiation ($\lambda = 1.54$ Å[45]), a scan speed of 600 s/step, and a step size of 0.02° over the 2θ range of 3−80°.

Electrochemical measurements (CV and RDE) were performed using a three-electrode glass cell, room-temperature 0.1 M HClO$_4$ electrolyte (GFS Chemicals, Inc.; 18 MΩ Millipore water) and a potentiostat (CH Instruments Model 760). The electrochemical cell included a Pt−Ni nanorod-coated GC disk working electrode of 0.196 cm^2 geometric surface area, a Pt wire counter electrode located in a separate fritted compartment, and a mercury/mercurous sulfate (Hg/Hg$_2$SO$_4$) reference electrode with a filling solution of 0.5 M H$_2$SO$_4$. The reference electrode was calibrated (reference potential = 0.713 V) against a reversible hydrogen electrode (RHE), and all potentials reported here are with respect to RHE. For CV measurements, the working electrodes were scanned between 0.01 and 1.1 V at a scan rate of 100 mV/s in argon (99.99% purity, Air Gas)-saturated 0.1 M HClO$_4$ to electrochemically clean (activate) the electrode surface. The activation was completed when the CV profile reached a steady state, typically after 50 cycles. The working electrodes were then scanned within the above potential range at 10 mV/s for two to three cycles to obtain CVs to be used for background subtraction and ECA determination. The working electrodes were also cycled numerous times in the 0.6−1.05 V range at 50 mV/s in argon-saturated 0.1 M HClO$_4$ to test the stability of the electrodes in the acidic environment. This test was followed by two cycles in the low potential range (0.6−0.01 V) to obtain the hydrogen adsorption (H_{upd}) charge used for estimating the ECA. The ECA losses were calculated by comparing the ECA values before and after the potential cycling. For the evaluation of ORR kinetics, CVs were recorded between 0.01 and 1.05 V at a scan rate of 10 mV/s in oxygen (99.99%, Air Gas)-saturated 0.1 M HClO$_4$ at room temperature and an electrode rotation speed of 1600 rpm. To eliminate the effect of pseudocapacitive currents on the calculated ORR activities, the background currents obtained using argon-saturated 0.1 M HClO$_4$ under identical conditions (i.e., room temperature and electrode rotation speed of 1600 rpm) were subtracted from the currents obtained in oxygen-saturated electrolyte. The reported ORR activities were obtained from the positive-going potential sweep of the CVs. After the electrochemical testing, the samples were analyzed using an FESEM (Hitachi S-4700-II

FESEM) with an EDX capability to obtain elemental composition of the leached Pt−Ni samples.

◼ RESULTS AND DISCUSSION

Figure 2 shows top and cross-sectional SEM images of the isolated, vertically aligned Pt−Ni nanorods with different Pt to
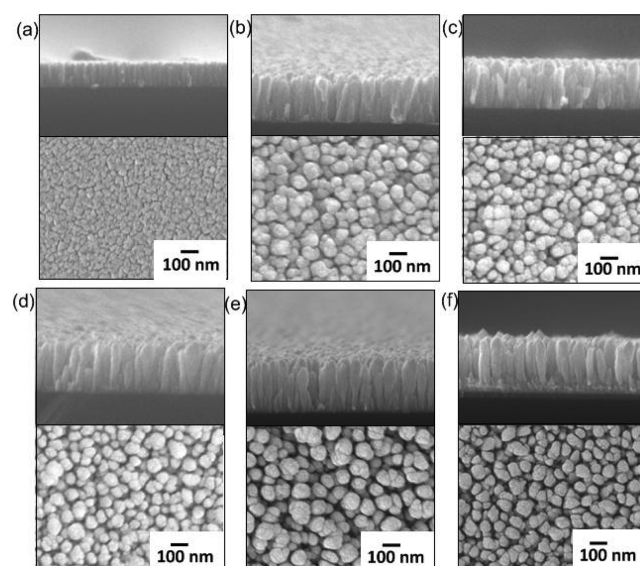
Figure 2. Cross-sectional and top SEM images of as-prepared nanorods with different Pt to Ni atomic ratios deposited on Si substrates: (a) monometallic Ni, (b) 1:8, (c) 1:3, (d) 1:2, (e) 1:1, and (f) monometallic Pt.

Ni atomic ratios. Images of monometallic Pt and Ni nanorods are also shown. As illustrated in Figure 2a, Ni does not form a well-isolated nanorod morphology. However, as the Pt content is increased, a more isolated morphology is achieved, which closely resembles that of pure Pt. The isolated nature of the alloy nanorods in the lateral direction leads to a channeled porosity aligned in the vertical direction to the substrate surface. This geometry can greatly help the effective transport of reactants to the catalyst sites in the electrode layer. By utilizing image processing software (SPIP, version 3.3.5.0), the average diameter and length of the nanorods were measured from the top and cross-sectional SEM images shown in Figure 2. The measured nanorod parameters are summarized in Table 1. It is noted that as the content of Ni in the nanorods is increased, the average diameter of the nanorods increases while the average length decreases. This is in agreement with the observation of less isolated morphology for the elemental nickel nanorods compared to those of elemental Pt nanorods, which may be attributed to the differences in surface free energy

Table 1. Measured Parameters for the Different Alloy Composition of Pt−Ni Nanorods on Si Substrates

nominal Pt:Ni (atomic ratio)	EDX Pt:Ni (atomic ratio)	XRD Pt:Ni (atomic ratio)	average diameter (nm)	average length (nm)	Pt loading (mg/cm^2) $\pm$ 0.005
1:1	1:1.2	(1:1.9)	50	230	0.105
1:2	1:2.2	(1:2.4)	50	210	0.076
1:3	1:3.5	(1:1.9)	60	200	0.058
1:8	1:8.2		75	200	0.029

density (Pt = 2.48 J/m^2, Ni = 1.70 J/m^2) leading to different growth rates for the different elemental crystal faces. In other words, Ni appears to have a sufficiently high surface diffusion to favor lateral growth. On the other hand, the shadowing effect overcomes the relatively low surface mobility on the Pt crystalline surfaces that leads to the formation of well-isolated vertical columnar nanostructures.[46]

The measured nanorod compositions, determined by EDX, closely matched the nominal compositions. The area weight loading of Pt in the Pt−Ni nanorods, as determined by QCM, was approximately 0.03, 0.06, 0.08, and 0.11 mg Pt/cm^2 for the nanorods with Pt to Ni atomic ratios of 1:8, 1:3, 1:2, and 1:1, respectively. These results indicate that by controlling the GLAD deposition parameters, such as target sputter power and deposition time, the composition of the Pt−Ni nanorods can be controlled, while closely maintaining the diameter (50−75 nm) and length (200−230 nm) of the nanorods, which are important factors in correlating the nanorod composition with catalytic activity.

The XRD patterns of the as-prepared Pt−Ni alloy nanorod arrays deposited on silicon substrates are shown in Figure 3. All
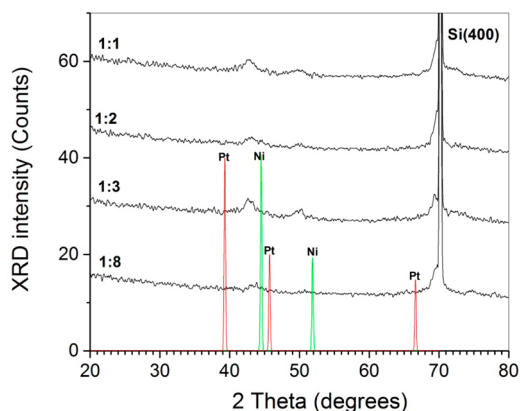

Figure 3. X-ray diffraction (XRD) profiles for the different Pt-to-Ni atom ratios of Pt−Ni nanorods deposited on Si wafers. Patterns are offset vertically for clarity. Marked peaks indicate two-theta positions for Pt and Ni from the database.

patterns show the ⟨400⟩ diffraction peak of the silicon wafer substrate. The remaining peaks in the pattern, though weak due to the low loading of material on the Si substrate, can be attributed to the nanorod reflections. Through comparison with the database for the monometallic systems (e.g., 2θ values of 39.76° ⟨111⟩, 46.24° ⟨200⟩, and 67.47° ⟨220⟩ for Pt (JCPDS-ICSD 4-802) and 44.49° ⟨111⟩, 51.85° ⟨200⟩, and 76.38° ⟨220⟩ for Ni (JCPDS-ICSD4-850)), no prominent peaks assignable to monometallic Pt or Ni are seen in the XRD patterns. The 2θ peaks for the ⟨111⟩ reflections of the 1:1, 1:2, and 1:3 Pt−Ni nanorods, though broadened due to the small size of the crystallites, show peak centers at approximately 42.6, 43.0, and 42.7°, intermediate between the 2θ values of the ⟨111⟩ reflections of pure Pt and Ni, indicating that the Pt and Ni have formed an alloy. By fitting the ⟨111⟩ peak, the d spacings in the 1:1, 1:2, and 1:3 Pt−Ni nanorods were calculated to be 2.12, 2.10, and 2.11 Å, respectively. It is noted that the 2θ peak for the ⟨111⟩ reflection of the 1:8 Pt−Ni nanorods is quite broad and extends into the 2θ position expected for the ⟨111⟩ reflection of monometallic Ni (44.49°). This is attributed to poor alloying in the nanorods with high Ni content, which is in agreement with the observation of less isolated morphology of

the monometallic Ni nanorods. Therefore, further analyses of the 1:8 Pt−Ni nanorods were not performed. The approximate Ni contents in the alloys calculated from these d spacings and using Vegard's law ($d_{PtNi} = Xd_{Pt} + (1 − X)d_{Ni}$, where X is the composition of Pt in the Pt−Ni nanorods and d_{PtNi}, d_{Pt}, and d_{Ni} are the d spacings of the ⟨111⟩ planes of PtNi, Pt, and Ni, respectively) are 63 atom % Ni, 71 atom % Ni, and 65 atom % Ni for the Pt−Ni nanorods with nominal Pt to Ni atomic ratios of 1:1, 1:2, and 1:3 (i.e., 50 atom % Ni, 67 atom % Ni, and 75 atom % Ni), respectively. The Ni atom % values determined by XRD are significantly higher than those determined by EDX for the 1:1 and 1:2 nanorods (i.e., 54.5 atom % Ni and 68.8 atom % Ni, respectively) and significantly lower than that determined by EDX for the 1:3 nanorods (77.8 atom % Ni). While this indicates existence of non-alloyed Pt in the 1:1 and 1:2 nanorods, and non-alloyed Ni in the 1:3 nanorods, the non-alloyed phases were not detectable in the XRD patterns, perhaps due to low loadings compared with the alloyed phase or to lack of crystallinity, especially if oxides are formed. Nevertheless, the XRD results show that a significant portion of the Pt is alloyed and that Pt and Ni can be alloyed at temperatures close to room temperature using the GLAD technique. The lowest alloying temperature of Pt−Ni reported in the literature is 300 °C.[47] Alloy formation at such low temperatures might be due to the preferential growth of crystalline phases/orientations with low adatom mobility (i.e., low surface diffusion) that were observed for GLAD nanostructures[46]. At the initial stages of GLAD growth, there is a random nucleation of islands of different crystal structures or orientations. In the case of GLAD Pt−Ni alloy nanorods, these alloy sites may have grown faster in vertical directions due to the lower adatom mobility at those sites. This may have been followed by the preferential growth of these alloy islands due to the shadowing effect during GLAD. Another possible origin of the low-temperature alloy formation might arise from the sputter deposition geometry (Figure 1). With the Pt and Ni sputter targets facing each other, there is the possibility of cross-deposition of Pt on the Ni target and vice versa. This also might have led to the formation of Pt−Ni alloy on the surface of sputter targets with the help of the high energy provided by the Ar ions bombarding the target surface.

As preparation for the ORR activity measurements using RDE, the nanorod-coated GC RDE disks were cycled between 0.01 and 1.1 V at a scan rate of 100 mV/s in deaerated 0.1 M HClO$_4$ electrolyte to electrochemically clean (activate) the electrode surface. During the potential cycling, the CV profile evolved toward one with features characteristic of a pure Pt surface, with the H_{upd} and hydrogen desorption peaks (0.06−0.40 V vs RHE), the double layer capacitive current plateau (0.4−0.6 V vs RHE), and the Pt hydroxide/oxide peaks (0.7−1.0 V vs RHE). The 5th, 7th, 10th, and 19th CV profiles of the 1:3 Pt−Ni nanorod electrode are shown in Figure 4 with arrows indicating the evolution of the CV features with potential cycling.

The arrows in Figure 4 indicate the decrease of the broad anodic and cathodic plateaus between 0.3 and 0.6 V concurrent with an increase of the hydrogen adsorption/desorption peaks during the potential cycling. The broad anodic plateau on the first CV scan likely indicates the presence of Ni on the nanorod surface, likely in the form of an oxide, whereas the hydrogen adsorption/desorption region indicates that Pt is also present on the nanorod surface. The dissolution of Ni is an irreversible process under the chosen potential conditions; any signs of Ni
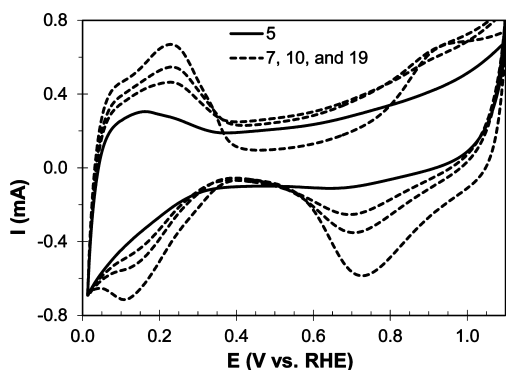
Figure 4. Cyclic voltammogram profiles for the activation of 1:3 Pt–Ni nanorod electrode. 5th (solid line); 7, 10, and 19th (dashed line) CV scans. 0.06–1.1 V vs RHE, 100 mV/s in deaerated 0.1 M HClO$_4$ at room temperature.

redeposition during the cathodic scan are absent. The activation of the Pt–Ni nanorod electrode, presumed to be caused by major dissolution of surface Ni, was completed when the CV profile reached steady state. During activation of the 1:8 Pt–Ni nanorod electrode, the CV profile did not reach steady state, and the nanorods were easily detached from the GC surface, presumably due to extensive etching of the nanorods from rapid dissolution of Ni in acid. Therefore, electrochemical testing of the 1:8 Pt–Ni electrode was not performed.

Figure 5 summarizes the results of the RDE studies for the activated Pt–Ni nanorod electrodes. Figure 5a shows the final CV profiles after activation in deaerated 0.1 M HClO$_4$ for the different Pt–Ni nanorod compositions. The CVs exhibit Pt-like H_{upd} features at potentials between 0.05 and 0.4 V that agree with those presented in the literature for nanoparticles and single crystal electrodes of Pt and Pt–Ni in acidic electrolyte.[17,48–50] The CVs from the Pt–Ni nanorods are somewhat

featureless in the hydrogen adsorption/desorption region compared to polycrystalline Pt, but they exhibit H_{upd} features attributable to the three low index planes of Pt. Generally, the peaks at approximately 0.11 V can be assigned to $\langle 110 \rangle$ and at 0.2–0.4 V to $\langle 100 \rangle$ surfaces.[48] The $\langle 111 \rangle$ terraces give a constant H_{upd} current over this region. The relatively featureless H_{upd} region for the nanorods may indicate a more significant contribution from the $\langle 111 \rangle$ terraces. The voltammetry for the three different nanorod compositions is similar, where the only notable difference is a less significant contribution from the $\langle 110 \rangle$ H_{upd} features for the 1:1 nanorods.

The ECA of the nanorod electrodes was determined by integrating the charge in the H adsorption region derived from CV profiles between the double-layer region and the onset of hydrogen evolution (0.05–0.4 V), after subtracting the double-layer charge and using the following equation to convert the measured charge to ECAs:[51]

$$
\text{ECA}_{\text{Pt,cat}} \ (\text{m}^2 \ \text{g}_{\text{Pt}}^{-1})
$$

$$
= \left[\frac{Q_{\text{H-adsorption}} \ (\text{C})}{210 \ (\mu\text{C cm}_{\text{Pt}}^{-2}) \ L_{\text{Pt}} \ (\text{mg}_{\text{Pt}} \ \text{cm}^{-2}) \ A_{\text{g}} \ (\text{cm}^2)} \right] 10^5
$$

$$(1)$$

where Q_{H} (210 μC/cm^2) is the charge of full coverage for clean polycrystalline Pt, $L_{\text{Pt,cat}}$ is the working electrode Pt loading (mg$_{\text{Pt}}$ cm^{-2}), and A_{g} is the geometric surface of the GC electrode (0.196 cm^2). The calculated ECAs are 23, 38, and 48 m^2/g$_{\text{Pt}}$, as determined from the nanorod surface areas 4.7, 5.6, and 5.5 cm^2 calculated from the H adsorption charges and the Pt loadings determined from QCM (see Table 1), for the 1:1, 1:2, and 1:3 nanorods, respectively. Given the nanorod diameters estimated from the SEM images shown in Figure 2 and assuming smooth nanorod surfaces, the expected ECA of Pt (i.e., the geometric surface area of the nanorods) was
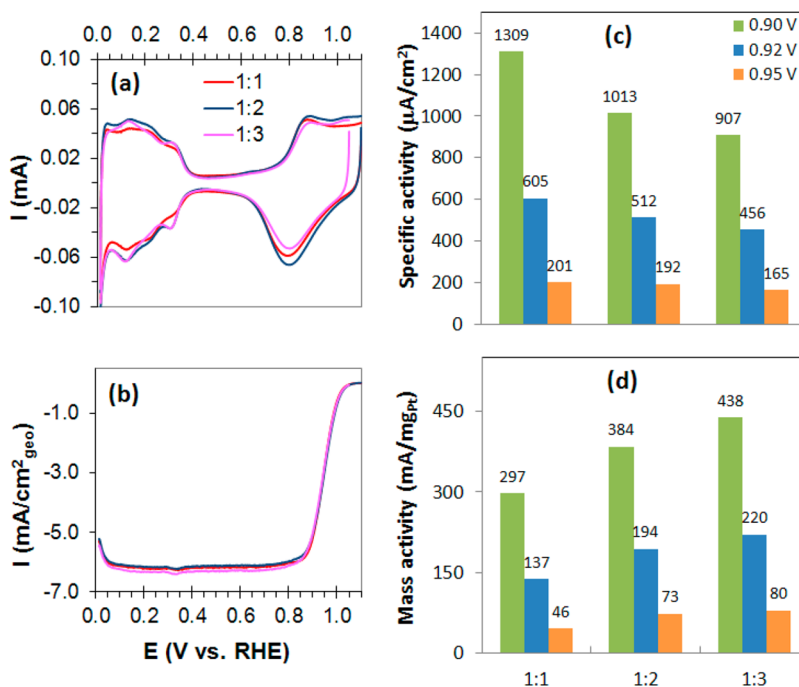
Figure 5. Electrochemical studies obtained by RDE for the Pt–Ni nanorod electrodes in 0.1 M HClO$_4$ at room temperature and 10 mV/s: (a) cyclic voltammograms in argon-saturated electrolyte; (b) background-corrected linear sweep voltammograms in O$_2$-saturated electrolyte, electrode rotation 1600 rpm; (c) area-specific activity; (d) mass activity of the Pt–Ni nanorods with different Pt to Ni atom ratios.

Table 2. Summary of the Measured Electrocatalytic Activity (SA and MA) at 0.9 V of Pt−Ni Nanorods in 0.1 M HClO₄ and Comparison to the Literature Values for Various Pt-Based Catalysts

method	sample	Pt loading (mg/cm^2)	ECA (m^2/g)	T (°C)	scan rate (mV/s)	SA (μA/cm^2)	MA (A/mg Pt)	ref
RDE	230 nm long 1:1 Pt−Ni nanorods	0.105, d = 50 nm	22.3	20	10	1309	0.30	this work
RDE	210 nm long 1:2 Pt−Ni nanorods	0.076, d = 50 nm	37.9	20	10	1013	0.38	this work
RDE	200 nm long 1:3 Pt−Ni nanorods	0.058, d = 50 nm	48.3	20	10	904	0.44	this work
RDE	200 nm long Pt nanorods	0.16	11	20	10	1080	0.13	11
RDE	Pt$_3$Ni poly annealed (727 °C), Pt overlayer			60	50	3342		56
RDE	Pt$_3$Ni/C octahedra	0.015, d = 10.6 nm		20	20	2700	0.11	19
RDE	Pt$_3$Ni/C cube	0.0102, d = 10.3 nm		20	20	521	0.04	19
RDE	PtNi/C	0.012, d = 5.0 nm		20		3900	1.56	20
RDE	PtNi$_2$/C	0.012, d = 5.0 nm		20		3600	1.31	20
RDE	PtNi$_3$/C	0.012, d = 5.0 nm		20		3300	0.92	20
MEA (50 cm^2 cell)	Pt$_3$Ni$_7$, 3 M NSTF	0.1		80		2250	0.28	12

estimated using the surface area of nanorods exposed to the electrolyte and the metal loading (from the EDX measured Pt to Ni ratios in Table 1). The expected ECA can be calculated using $((\pi r^2 + 2\pi rh)((g_{Pt} + g_{Ni})/\pi r^2 h\rho))/g_{Pt}$, where r is the radius of the nanorod, h is the height of the nanorod, ρ is the mass density, determined from the Pt to Ni atomic ratio, of the nanorods, and g is grams of the indicated metal. The expected ECAs calculated using this equation are 7.6, 10.8, and 12.2 m^2/g$_{Pt}$ for the nanorods with nominal Pt to Ni ratios of 1:1, 1:2, and 1:3, respectively. The measured ECAs are more than a factor of 3 higher than the expected ECAs, and the ratio of measured ECA to expected ECA increases with increasing ratio of Ni to Pt in the as-prepared nanorods. Considering the well-controlled and uniform nanorod size (diameter and length) and the well-controlled Pt−Ni composition, the high values of the measured ECA may be attributed to a roughened nanorod surface. It can be speculated that leaching of Ni atoms out of the surface and/or near surface region of the nanorods results in surface roughening and in a larger number of Pt surface sites relative to a smooth nanorod of the same diameter.[52] The loss of Ni is not unexpected, since the surface Ni will be dissolved when the alloy nanorods are exposed to the acidic electrolyte and potential cycling, forming a Pt-skeleton (leached-out) surface.[52,53] Indeed, the 1:3 Pt−Ni nanorod electrode, with its higher Ni content, required a large number of activation CVs compared to the 1:1 and 1:2 Pt−Ni nanorod electrodes for the CV profile to reach steady state.

The ORR activity of the nanorod electrodes was determined using the RDE technique and CVs taken at 10 mV/s in O₂-saturated 0.1 M HClO₄. The anodic-going traces of these CVs are shown in Figure 5b. The onset of ORR occurred at 1.05 V for all the Pt−Ni nanorod compositions, and the CVs exhibit the typical mixed kinetic-diffusion controlled region from 0.8 to 1.0 V and diffusion-limited current region from 0.4 to 0.8 V. The diffusion-limited currents for all the Pt−Ni nanorod electrodes, normalized to the RDE tip area, are within 10% of what is theoretically expected (5.7 mA/cm^2) for a rotation rate of 1600 rpm, O₂-saturated room temperature electrolyte, and a four-electron reduction, which indicates uniform and complete coverage of the GC disks with catalyst and minimal effects of inhibition of oxygen diffusion through the thickness of the nanorod layer.[4,51,54] The RDE traces are nearly identical for the different Pt−Ni nanorod compositions with identical half-wave

potentials (i.e., the potential at which the current is half that of the diffusion-limited current) of 0.946 V.

The ORR electrocatalytic activity for the Pt−Ni nanorod electrodes is reported as area- and mass-specific activities using the ORR kinetic current derived from the CV traces and utilizing the well-known mass-transport correction for RDE measurements:[4,51,54]

$$i_k = (i_{lim} * i)/(i_{lim} - i) \qquad (2)$$

where i_k is the kinetic current, i_{lim} is the measured limiting current at 0.5 V vs RHE, and i is the measured current at a specific potential. It should be noted that the assumptions for extracting i_k from the RDE data using eq 2 are valid over the current range of $0.1 i_{lim} < i < 0.8 i_{lim}$, and the accuracy of the extracted kinetics decrease as the diffusion-limited value is approached.[54] When the current is affected by mass transport, the calculated kinetic currents are lower than the true kinetic currents. For the 1:1 and 1:2 Pt−Ni nanorod electrodes, the measured current at 0.9 V ($i_{0.9V}$ = 1010 and 992 μA, respectively) is slightly greater than 80% of the measured limiting current ($0.8 i_{lim}$ = 968 and 960 μA, respectively). Therefore, kinetic currents were also calculated for higher potentials as well (0.92 and 0.95 V) to provide for a more robust assessment of electrocatalytic activity. The SA and MA are derived by normalizing kinetic currents, calculated from eq 2, by the ECA and the Pt loading of the catalyst applied to the electrode, respectively, and measured as described previously. Parts c and d of Figure 5, respectively, show the calculated SA and MA of the different Pt−Ni nanorod electrodes. As a result of the nanorod composition variation, a linear trend was obtained for the SA and MA dependence on the alloy composition of the nanorod electrodes (Figures 5c,d). The SA monotonically decreases with increasing Ni content (1:1 Pt−Ni > 1:2 Pt−Ni > 1:3 Pt−Ni), while the MA monotonically increases with increasing Ni content (1:1 Pt−Ni < 1:2 Pt−Ni < 1:3 Pt−Ni) at 0.9, 0.92, and 0.95 V. Two possible causes of the observed SA trend with decreasing Pt-to-Ni ratio are an increasing number of low-coordinated Pt sites, formed by the dissolution of Ni from the near-surface region, with increasing initial Ni content of the nanorods or greater retention of Ni after the activation procedure with increasing Pt content in the nanorods.[14,55] Low-coordinated Pt sites have been shown to have lower intrinsic ORR activity than sites with higher coordination.[17] The 1:1 nanorods also showed more of a ⟨111⟩

signature in the CVs, and this crystal face has been shown to be the most active for ORR for Pt−Ni alloys.[20,] The MA trend is consistent with the Pt loading in the nanorods: the three electrodes have approximately the same ORR kinetic current, as shown in Figure 5b, but the loading of Pt on the RDE tip decreased with increasing nanorod Ni content (Table 1).

By comparing the measured SA (1309, 1013, and 907 μA/cm^2 at 0.9 V) for the 1:1, 1:2, and 1:3 Pt−Ni nanorods, respectively, with the SA (1080 μA/cm^2) of monometallic Pt nanorods of similar size (length of 200 nm and diameter of 50 nm), as reported previously,[11] the nominal 1:1 Pt−Ni nanorods showed a SA enhancement of 21%, while the nominal 1:2 and 1:3 nanorods showed a SA decrease of 6 and 16%, respectively. This indicates that some fraction of the Ni is retained in the near surface region of the 1:1 Pt−Ni nanorods after electrochemical cycling or that the lattice compression effects of Ni are retained in the catalysts after chemical and electrochemical removal of the Ni (i.e., dealloying) and are influencing the ORR SA of the Pt on the surface of the nanorods.[13] The 1:2 and 1:3 Pt−Ni alloys may have most of their Ni leached from the near surface region of the nanorods due to Ni percolation pathways from the interior of the nanorod to the solution.[14,55] The Pt−Ni alloy nanorods also show high MA compared to that of monometallic Pt nanorods (0.13 A/mg$_{Pt}$) with enhancement factors of 2.3, 3.0, and 3.5 for the nominal 1:1, 1:2, and 1:3 Pt−Ni, respectively. The MA enhancement for the nominal 1:1 Pt−Ni nanorods can be attributed to both substitution of Ni for Pt in the interior of the nanorods and to enhancement of the ORR activity on a per surface Pt basis, as noted previously in the ORR SA results. The MA enhancement for the nominal 1:2 and 1:3 Pt−Ni nanorods can be attributed to roughening of the nanorod surface, presumably due to Ni leaching, increasing the number of surface Pt sites per geometric area of electrode, and to substitution of Ni for Pt in the interior of the nanorods.

A review of ORR activities for Pt−Ni catalyst systems reported in the literature (Table 2) shows that the enhancement of ORR activity is a function of the relative abundance of active surface planes ($\langle 111 \rangle$, $\langle 110 \rangle$, and $\langle 100 \rangle$) and increases in the order $\langle 100 \rangle < \langle 110 \rangle \ll \langle 111 \rangle$.[21,19,29,58] Zhang et al.[19] obtained SA for carbon-supported Pt$_3$Ni nanocube particles that is approximately a factor of 1.7−2.5 lower than the SA of the Pt−Ni nanorods. The nanocube particles exhibited Pt features typical of $\langle 100 \rangle$ surface planes and hence showed relatively low ORR activity.[17] Stamenkovic et al. obtained SA for polycrystalline extended Pt$_3$Ni covered with a Pt overlayer that is approximately a factor of 2.5 or more higher than the SA of the Pt−Ni nanorods.[56] The observed enhancement reported by Stamenkovic et al. is based on the surface enrichment of Pt atoms as a result of the surface segregation phenomenon, induced by heat treatments, that results in a system in which a strong enrichment of Pt in the alloy systems is counterbalanced by the depletion of Pt in the first two or three layers. In addition, the extended Pt$_3$Ni electrodes have been shown to exhibit an abundance of the more ORR active $\langle 111 \rangle$ surfaces and suppression of the less active $\langle 100 \rangle$ surfaces.[17] Zhang et al. also obtained SA for carbon-supported Pt$_3$Ni nano-octahedra particles that are approximately a factor of 2−3 higher than the SA of the Pt−Ni nanorods of this work.[19] The nano-octahedra particles exhibited Pt features that resembled those of an extended Pt$_3$Ni $\langle 111 \rangle$ surface, and hence the enhanced ORR activity.[17] In another example, Wang et al. obtained SA for a carbon-supported Pt−Ni nanoparticle (PtNi/C) catalyst[20] that

is a factor of 3 or more higher than the SA of Pt−Ni nanorods, which was attributed to an abundance of the $\langle 111 \rangle$ surface. The Pt−Ni nanorods of this work showed a mixed contribution from all the crystal surfaces in the background CVs (i.e., $\langle 111 \rangle$, $\langle 110 \rangle$, and $\langle 100 \rangle$), with the 1:2 and 1:3 Pt−Ni showing more of the $\langle 100 \rangle$ feature than the 1:1 Pt−Ni, consistent with the higher activity enhancement for the 1:1 than for the 1:2 and 1:3 Pt−Ni.

The stability of the ECA and ORR activity of the nanorods with potential cycling was determined to evaluate the potential durability of the Pt−Ni nanorod electrodes during PEFC load cycling. Figure 6 summarizes the measured ECA trends
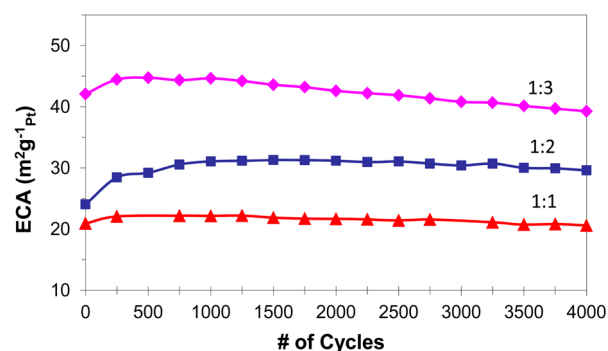
Figure 6. Comparison of ECA for the Pt−Ni nanorod electrodes with different Pt to Ni atom ratios during the potential cycling (0.6−1.05 V, 50 mV/s, 900 rpm, Ar-saturated 0.1 M HClO$_4$, room temperature).

observed during the potential cycling. The ECA of all the Pt−Ni nanorod electrodes increased during the first 1000 cycles, and an ECA decrease was observed after 1000 cycles. The increasing ECA during the first 1000 potential cycles likely comes from an increasing nanorod surface roughness resulting from the dissolution of Ni from the nanorods. Beyond 1000 cycles, the small but notable decrease in ECA is likely caused by the collapse and/or rearrangement of the dealloyed nanorod surface or dissolution of Pt adatoms.

Figure 7 summarizes the electrochemical results for the Pt−Ni nanorod electrodes before and after 4000 voltage cycles between 0.6 and 1.05 V. Parts a−c of Figure 7 compare the initial CV to the final CV in O$_2$-free electrolyte after stability testing for the three electrodes with different Pt to Ni ratios. The H_{upd} peak positions remain the same after stability testing. However, it is notable that the intensity at ∼0.20 V is decreased after stability testing and that the decrease is more pronounced for the nominal 1:2 Pt−Ni nanorods than for the nominal 1:1 and 1:3 Pt−Ni nanorods. These changes could indicate preferential faceting of the nanorods with enhancement of the $\langle 100 \rangle$ surface planes. Figure 7d shows that the ECA values decreased slightly: from 23 to 22 m^2 g$_{Pt}$$^{-1}$ (0.7%) for the 1:1 Pt−Ni, from 38 m^2 g$_{Pt}$$^{-1}$ to 33 m^2 g$_{Pt}$$^{-1}$ (4.7%) for the 1:2 Pt−Ni, and from 48 m^2 to 44 m^2 g$_{Pt}$$^{-1}$ (4.0%) for the 1:3 Pt−Ni. Overall, all the Pt−Ni nanorod electrodes had minor losses (<5%) in ECA after 4000 potential cycles in comparison to a substantial drop of 40% for Pt/C sample after 1000 potential cycles and 37% for 200 nm long Pt nanorods after 4500 potential cycles observed in our earlier studies on Pt nanorods.[11] Figure 7e shows the ORR SA determined at 0.92 V for the Pt−Ni nanorod electrodes before and after stability test experiments. All the Pt−Ni nanorod electrodes showed a decrease in SA after stability testing, with the 1:1 electrode showing greater loss (39%) than 1:2 (17%) and 1:3
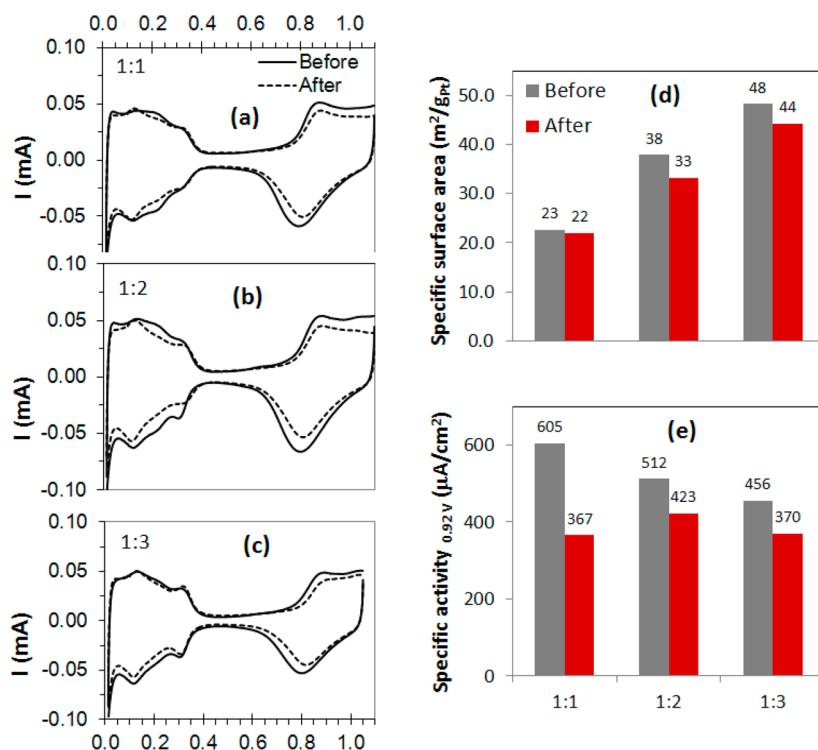
Figure 7. Summary of electrochemical stability studies obtained by RDE before and after 4000 potential cycles between 0.6 and 1.05 V for the Pt−Ni nanorod electrodes in 0.1 M HClO$_4$ at 0.92 V and room temperature: (a−c) cyclic voltammograms; (d) specific surface area; (e) ORR specific activity. Estimation of ECA was based on integrated H_{upd} for the Pt−Ni nanorod electrodes.

(19%). It is likely that the 1:2 and 1:3 Pt−Ni nanorods have almost all of the Ni leached out of the near surface region of the nanorods prior to the stability test and additional cycling does not cause much of a change in ORR activity. The 1:1 Pt−Ni nanorod may have retained a significant portion of the Ni after the initial exposure to acid and additional cycling caused further leaching and loss of ORR activity.

EDX analysis was performed on the Pt−Ni nanorod electrodes after the electrochemical testing and stability testing to determine the Pt and Ni composition. It was found that the composition had changed substantially as compared to the initial values, with much less Ni in the nanorods after electrochemical testing than in the as-prepared nanorods. The Ni composition in the nanorods decreased from 54.5, 68.9, and 77.8 atom % in the as-prepared nanorods to 26.3, 19.5, and 13.5 atom % for the nominal 1:1, 1:2, and 1:3 Pt−Ni nanorods, respectively. The loss of Ni increases with increasing initial Ni content, showing an inverse linear relationship between initial and final Ni content which results in the nominal 1:1 Pt−Ni nanorod catalyst having the highest final Ni content of the three nanorod catalysts tested. At this point, we can speculate that ORR activity loss with cycling is associated with the decreased effect of Ni on the ORR activity of Pt, which, as mentioned previously, has been postulated in the literature to arise from compressive surface lattice strain of the Pt surface lattice induced by alloying with Ni.[13,53,57,58]

■ CONCLUSION

The glancing angle deposition (GLAD) technique was used to grow vertically aligned platinum−nickel nanorod arrays on glassy carbon electrodes. By controlling the GLAD deposition parameters, such as target sputter power and deposition time, the composition of Pt−Ni nanorods can be controlled while closely maintaining the diameter and length of the nanorods; the Pt to Ni atomic ratios studied were 1:1, 1:2, 1:3, and 1:8. It was determined by XRD that the GLAD technique results in alloying of the Pt and Ni. The GLAD Pt−Ni nanorod electrodes were investigated as potential ORR electrocatalysts for PEFCs using CV and RDE techniques in room-temperature aqueous dilute perchloric acid electrolyte to determine their ORR activities and stabilities with extensive potential cycling as would be encountered during PEFC load cycling. After initial potential cycling to activate the catalysts, the Pt−Ni nanorods showed CV features characteristic of the three low-index crystal planes of Pt (i.e., ⟨111⟩, ⟨110⟩, and ⟨100⟩), with the 1:2 and 1:3 Pt−Ni nanorods showing more prominent ⟨100⟩ features than the 1:1 Pt−Ni nanorods. Comparison of the calculated geometric surface area to the initial measured ECA of the nanorod electrodes showed that the nanorod surface roughness increased with increasing as-prepared Ni content, presumably due to increased leaching of Ni from the nanorods.

The initial area-specific ORR activity of the nanorods increased in the order 1:3 < 1:2 < 1:1, with the 1:1 nanorods showing an area-specific ORR enhancement of 21% as compared to Pt nanorods of approximately the same dimentions. It was speculated that the higher initial ORR SA for the 1:1 catalyst was due to greater resistance to loss of Ni upon exposure to the acidic electrolyte and short-term potential cycling and a larger predominance of the intrinsically more active ⟨111⟩ crystal face on these nanorods. The Pt mass-specific ORR activity of the Pt−Ni nanorods was found to be a factor of 2.3−3.5 higher than that of pure Pt nanorods of the same dimensions and to increase with increasing Ni content of the nanorods.

The ECA of the nanorods was relatively stable with extended (4000 cycles) potential cycling between 0.6 and 1.05 V as

compared to the Pt nanorods of comparable dimensions reported in our previous study and as compared to standard carbon-supported nanoparticle Pt. The nanorods were observed to lose ORR SA with cycling concomitant with loss of Ni, as measured by pre- and post-cycling EDX. This study provides the baseline for further improvement in the ORR activity and ORR activity stability of these materials using additional engineering approaches in the GLAD technique, such as deposition of a thin film coating of Pt on the alloy nanorods to retain Ni in the nanorod core. In addition, as the nanorods are not supported, post-deposition thermal annealing to drive surface segregation of Pt is possible. Future studies will also focus on control of deposition parameters to promote the growth of the preferred crystallographic orientations for ORR. These approaches may open the way for utilizing GLAD to develop unsupported nanostructures with controllable area density, spacing, base metal content, and crystallographic orientation as cathode catalyst in PEFCs.

■ AUTHOR INFORMATION

Corresponding Author
*E-mail: kariuki@anl.gov.

Notes
The authors declare no competing financial interest.

■ ACKNOWLEDGMENTS

■ REFERENCES

(1) Eikerling, M. H.; Malek, K.; Wang, Q. In *PEM fuel cell electrocatalysts and catalyst layer-fundamentals and applications*; Zhang, J., Ed.; Springer-Verlag: London, 2008.

(2) Wagner, F. T.; Lakshmanan, B.; Mathias, M. F. *J. Phys. Chem. Lett.* **2010**, *1*, 2204−2219.

(3) Borup, R.; Meyers, J.; Pivovar, B.; Kim, Y. S.; Mukundan, R.; Garland, N.; Myers, D.; Wilson, M.; Garzon, F.; Wood, D.; Zelenay, P.; More, K.; Stroh, K.; Zawodzinski, T.; Boncella, J.; McGrath, J. E.; Inaba, M.; Miyatake, K.; Hori, M.; Ota, K.; Ogumi, Z.; Miyata, S.; Nishikata, A.; Siroma, Z.; Uchimoto, Y.; Yasuda, K.; Kimijima, K. I.; Iwashita, N. *Chem. Rev.* **2007**, *107*, 3904−3951.

(4) Gasteiger, H. A.; Kocha, S. S.; Sompalli, B.; Wagner, F. T. *Appl. Catal., B* **2005**, *56*, 9−35.

(5) Tang, H.; Qi, Z. G.; Ramani, M.; Elter, J. F. *J. Power Sources* **2006**, *158*, 1306−1312.

(6) Qiao, J. L.; Saito, M.; Hayamizu, K.; Okada, T. *J. Electrochem. Soc.* **2006**, *153*, A967−A974.

(7) Gasda, M. D.; Eisman, G. A.; Gall, D. *J. Electrochem. Soc.* **2010**, *157*, B71−B76.

(8) Bonakdarpour, A.; Fleischauer, M. D.; Brett, M. J.; Dahn, J. R. *Appl. Catal., A* **2008**, *349*, 110−115.

(9) Khudhayer, W. J.; Kariuki, N.; Myers, D. J.; Shaikh, A. U.; Karabacak, T. *J. Electrochem. Soc.* **2012**, *159*, B729−B736.

(10) Khudhayer, W. J.; Shaikh, A. U.; Karabacak, T. *Adv. Sci. Lett.* **2011**, *4*, 3551−3559.

(11) Khudhayer, W. J.; Kariuki, N. N.; Wang, X. P.; Myers, D. J.; Shaikh, A. U.; Karabacak, T. *J. Electrochem. Soc.* **2011**, *158*, B1029−B1041.

(12) Debe, M. K.; Steinbach, A. J.; Vernstrom, G. D.; Hendricks, S. M.; Kurkowski, M. J.; Atanasoski, R. T.; Kadera, P.; Stevens, D. A.; Sanderson, R. J.; Marvel, E.; Dahn, J. R. *J. Electrochem. Soc.* **2011**, *158*, B910−B918.

(13) Strasser, P.; Koh, S.; Anniyev, T.; Greeley, J.; More, K.; Yu, C. F.; Liu, Z. C.; Kaya, S.; Nordlund, D.; Ogasawara, H.; Toney, M. F.; Nilsson, A. *Nat. Chem.* **2010**, *2*, 454−460.

(14) Snyder, J.; McCue, I.; Livi, K.; Erlebacher, J. *J. Am. Chem. Soc.* **2012**, *134*, 8633−8645.

(15) Gan, L.; Heggen, M.; O'Malley, R.; Theobald, B.; Strasser, P. *Nano Lett.* **2013**, *13*, 1131−1138.

(16) Stamenkovic, V. R.; Mun, B. S.; Arenz, M.; Mayrhofer, K. J. J.; Lucas, C. A.; Wang, G. F.; Ross, P. N.; Markovic, N. M. *Nat. Mater.* **2007**, *6*, 241−247.

(17) Stamenkovic, V. R.; Fowler, B.; Mun, B. S.; Wang, G. F.; Ross, P. N.; Lucas, C. A.; Markovic, N. M. *Science* **2007**, *315*, 493−497.

(18) Greeley, J.; Norskov, J. K. *J. Phys. Chem. C* **2009**, *113*, 4932−4939.

(19) Zhang, J.; Yang, H. Z.; Fang, J. Y.; Zou, S. Z. *Nano Lett.* **2010**, *10*, 638−644.

(20) Wang, C.; Chi, M. F.; Wang, G. F.; van der Vliet, D.; Li, D. G.; More, K.; Wang, H. H.; Schlueter, J. A.; Markovic, N. M.; Stamenkovic, V. R. *Adv. Funct. Mater.* **2011**, *21*, 147−152.

(21) Wadayama, T.; Todoroki, N.; Yamada, Y.; Sugawara, T.; Miyamoto, K.; Iijama, Y. *Electrochem. Commun.* **2010**, *12*, 1112−1115.

(22) Nesselberger, M.; Ashton, S.; Meier, J. C.; Katsounaros, I.; Mayrhofer, K. J. J.; Arenz, M. *J. Am. Chem. Soc.* **2011**, *133*, 17428−17433.

(23) Debe, M. K. *Nature* **2012**, *486*, 43−51.

(24) Debe, M. K.; Poirier, R. J. *J. Vac. Sci. Technol., A* **1994**, *12*, 2017−2022.

(25) Debe, M. K. In *Handbook of Fuel Cells—Fundamentals, Technology and Applications*; Vielstich, W., Lamm, A., Gasteiger, H. A., Eds.; John Wiley & Sons: New York, 2003; Chapter 45.

(26) Bonakdarpour, A.; Stevens, K.; Vernstrom, G. D.; Atanasoski, R.; Schmoeckel, A. K.; Debe, M. K.; Dahn, J. R. *Electrochim. Acta* **2007**, *53*, 688−694.

(27) Steinbach, A. J.; Debe, M. K.; Pejsa, M. J.; Peppin, D. M.; Haug, A. T.; Kurkowski, M. J.; Hendricks, S. M. *ECS Trans.* **2011**, *41*, 449−457 (Polymer Electrolyte Fuel Cells 11).

(28) Debe, M. K.; Drube, A. R. *J. Vac. Sci. Technol., B* **1995**, *13*, 1236−1241.

(29) Van der Vliet, D. F.; Wang, C.; Tripkovic, D.; Strmcnik, D.; Zhang, X. F.; Debe, M. K.; Atanasoski, R. T.; Markovic, N. M.; Stamenkovic, V. R. *Nat. Mater.* **2012**, *11*, 1051−1058.

(30) Shui, J. I.; Chen, C.; Li, J. C. M. *Adv. Funct. Mater.* **2011**, *21*, 3357−3362.

(31) Liu, L. F.; Pippel, E. *Angew. Chem., Int. Ed.* **2011**, *50*, 2729−2733.

(32) Cui, C. H.; Li, H. H.; Yu, J. W.; Gao, M. R.; Yu, S. H. *Angew. Chem., Int. Ed.* **2010**, *49*, 9149−9152.

(33) Zhou, H. J.; Zhou, W. P.; Adzic, R. R.; Wong, S. S. *J. Phys. Chem., C* **2009**, *113*, 5460−5466.

(34) Chen, Z. W.; Waje, M.; Li, W. Z.; Yan, Y. S. *Angew. Chem., Int. Ed.* **2007**, *46*, 4060−4063.

(35) Karabacak, T.; Wang, G. C.; Lu, T. M. *J. Vac. Sci. Technol., A* **2004**, *22*, 1778−1784.

(36) Gasda, M. D.; Teki, R.; Lu, T. M.; Koratkar, N.; Eisman, G. A.; Gall, D. *J. Electrochem. Soc.* **2009**, *156*, B614−B619.

(37) Gasda, M. D.; Eisman, G. A.; Gall, D. *J. Electrochem. Soc.* **2010**, *157*, B437−B440.

(38) Gasda, M. D.; Eisman, G. A.; Gall, D. *J. Electrochem. Soc.* **2010**, *157*, B113−B117.

(39) He, Y. P.; Zhao, Y. P. *Nanoscale* **2011**, *3*, 2361−2375.

(40) Markovic, N. M.; Ross, P. N. *Surf. Sci. Rep.* **2002**, *45*, 121−229.

(41) He, Y. P.; Brown, C.; Lundgren, C. A.; Zhao, Y. P. *Nanotechnology* **2012**, *23*, 365703.

(42) Zhao, Y. P.; He, Y. P.; Brown, C. *Appl. Phys. Lett.* **2012**, *100*, 033106.

(43) He, Y. P.; Zhao, Y. P.; Wu, J. S. *Appl. Phys. Lett.* **2008**, *92*, 063107.

(44) Krause, K. M.; Taschuk, M. T.; Brett, M. J. *J. Vac. Sci. Technol., A* **2013**, *31*, 31507−31501.

(45) Holzer, G.; Fritsch, M.; Deutsch, M.; Hartwig, J.; Forster, E. *Phys. Rev., A* **1997**, *56*, 4554−4568.

(46) Karabacak, T.; Mallikarjunan, A.; Singh, J. P.; Ye, D. X.; Wang, G. C.; Lu, T. M. *Appl. Phys. Lett.* **2003**, *83*, 3096−3098.

(47) Park, K. W.; Choi, J. H.; Sung, Y. E. *J. Phys. Chem. B* **2003**, *107*, 5851−5856.

(48) Vidal-Iglesias, F. J.; Aran-Ais, R. M.; Solla-Gullon, J.; Herrero, E.; Feliu, J. M. *ACS Catal.* **2012**, *2*, 901−910.

(49) Van der Vliet, D.; Wang, C.; Debe, M.; Atanasoski, R.; Markovic, N. M.; Stamenkovic, V. R. *Electrochim. Acta* **2011**, *56*, 8695−8699.

(50) Wang, C.; Chi, M. F.; Li, D. G.; Strmcnik, D.; Van der Vliett, D.; Wang, G. F.; Komanicky, V.; Chang, K. C.; Paulikas, A. P.; Tripkovic, D.; Pearson, J.; More, K. L.; Markovic, N. M.; Stamenkovic, V. R. *J. Am. Chem. Soc.* **2011**, *133*, 14396−14403.

(51) Garsany, Y.; Baturina, O. A.; Swider-Lyons, K. E.; Kocha, S. S. *Anal. Chem.* **2010**, *82*, 6321−6328.

(52) Watanabe, M.; Tsurumi, K.; Mizukami, T.; Nakamura, T.; Stonehart, P. *J. Electrochem. Soc.* **1994**, *141*, 2659−2668.

(53) Stamenkovic, V. R.; Mun, B. S.; Mayrhofer, K. J. J.; Ross, P. N.; Markovic, N. M. *J. Am. Chem. Soc.* **2006**, *128*, 8813−8819.

(54) Mayrhofer, K. J. J.; Blizanac, B. B.; Arenz, M.; Stamenkovic, V. R.; Ross, P. N.; Markovic, N. M. *J. Phys. Chem. B* **2005**, *109*, 14433−14440.

(55) Carlton, C. E.; Chen, S.; Ferreira, P. J.; Allard, L. F.; Shao-Horn, Y. *J. Phys. Chem. Lett.* **2012**, *3*, 161−166.

(56) Stamenkovic, V.; Mun, B. S.; Mayrhofer, K. J. J.; Ross, P. N.; Markovic, N. M.; Rossmeisl, J.; Greeley, J.; Norskov, J. K. *Angew. Chem., Int. Ed.* **2006**, *45*, 2897−2901.

(57) Yang, R. Z.; Leisch, J.; Strasser, P.; Toney, M. F. *Chem. Mater.* **2010**, *22*, 4712−4720.

(58) Mun, B. S.; Watanabe, M.; Rossi, M.; Stamenkovic, V.; Markovic, N. M.; Ross, P. N. *Surf. Rev. Lett.* **2006**, *13*, 697−702.